Three-dimensional numerical study of natural convection in vertical cylinders partially heated from the side.

D. J. Ma, Daniel Henry, Hamda Ben Hadid

To cite this version:

D. J. Ma, Daniel Henry, Hamda Ben Hadid. Three-dimensional numerical study of natural convection in vertical cylinders partially heated from the side.. Physics of Fluids, 2005, 17, pp.124101 : 1-12. 10.1063/1.2141430 . hal-00077464

Three-dimensional numerical study of natural convection in vertical cylinders partially heated from the side

D. J. Ma, D. Henry and H. BenHadid
Laboratoire de Mécanique des Fluides et d'Acoustique, UMR CNRS 5509,
Ecole Centrale de Lyon/Université Claude Bernard Lyon 1/INSA de Lyon
ECL, 36 avenue Guy de Collongue, 69134 Ecully Cedex, France

(October 2005)

Abstract

Three-dimensional steady and oscillatory flows are simulated in a vertical cylinder partially heated from the side. The vertical wall is heated in a zone at mid-height and is insulated above and below this middle zone, while both ends of the cylinder are cooled. The cylinder aspect ratio (A = height/radius) ranges from 2 to 8, whereas a fixed Prandtl number, $Pr = 0.021$, is considered as well as a fixed length of the heated zone, equal to the cylinder radius. Three-dimensional steady and unsteady simulations as well as mode decomposition techniques and energy transfer analyses are used to characterize the flows and their transitions. The flows that develop from the steady toroidal pattern beyond the first instability threshold, break the axisymmetry. At small A ($2 \leq A \leq 2.5$), the flow corresponds to a two-roll rotating pattern which is triggered by a $k = 2$ azimuthal mode as a result of a hydrodynamic instability. At large A ($3 \leq A \leq 8$), the flow is steady and corresponds to a main one-roll pattern in the upper part of the cylinder. The flow is triggered by a $k = 1$ mode as a result of buoyancy effects affecting this unstably stratified upper part (Rayleigh-Bénard instability), but shear effects are involved in the instability for the smaller values of A.

These steady flows then transit at a higher threshold to a standing wave oscillatory one-roll pattern associated with the breaking of symmetry of the previous steady pattern. For intermediate values of A ($2.7 \leq A \leq 2.9$), the transition is towards an oscillatory pattern, but hysteresis phenomena with multiplicity of steady and oscillatory states have been found. Comparisons with experiments performed at aspect ratios $A = 4$ and $A = 8$ are then considered and discussed.

I. INTRODUCTION

Natural convection occuring in the melt during crystal growth processes has been widely studied (see reviews in Refs[1,2]) since it has been known that the melt flow can significantly affect the homogeneity of the grown crystal. The transition to time dependent convection is especially problematic because it can induce undesirable periodic inhomogeneities (also known as striations) in the crystals. Among the numerous convection studies, several of them have focused on the convection induced in heated vertical circular cylinders as it is a basic configuration of several crystal growth systems as vertical Bridgman growth or vertical zone melting. The basic studies started with the Rayleigh-Bénard configuration in vertical cylinders heated from below[3–6]. This situation proved to be particularly rich in pattern transitions as the temperature difference is increased, from the onset of convection to oscillatory flow transition through steady transitions with symmetry breakings. More complicated, but more realistic heating conditions have also been considered such as parabolic temperature distributions on the cylindrical sidewall[7,8]. It was found that the axisymmetry breaking of convection or the transition to oscillatory flow occur beyond certain values of the Rayleigh number (Ra) and these critical values of Ra strongly depend on the cylinder aspect ratio. More specific heating conditions have been recently used in order to investigate convection in a simulated vertical zone melting configuration[9–11]: they correspond to a local heating in an axial band at the mid-height of the cylinder. The experimental work of Selver *et al.*[9] has shown different oscillatory transitions depending on the aspect ratio, either direct transitions, or transitions through a first steady transition. The two-dimensional work of Erenburg *et al.*[10] has revealed complicated bifurcation diagrams and the existence of multiple solutions. At last, the recently published paper of Rubinov *et al.*[11] has carefully studied the transition leading to the three-dimensional axisymmetry breaking of the flow. They have presented the dependence of the critical Grashof number on the aspect ratio and have shown that three different modes are the most dangerous perturbations and that they replace each other with the variation of the aspect ratio.

In this paper, three-dimensional calculations are performed in order to simulate the experimental configuration proposed by Selver *et al.*[9], i. e., a vertical cylinder partially heated from the side. In the model, the vertical wall is heated in a zone at the mid-height of the cylinder and is insulated above and below this middle zone while both ends of the cylinder are cooled. The cylinder aspect ratio (A = height/radius) ranges from 2 to 8, whereas a fixed Prandtl number, $Pr = 0.021$, is considered as well as a fixed length of heated zone, equal to the cylinder radius. Our study is a continuation of the work of Rubinov *et al.*[11]: by linear stability analysis, they have determined the thresholds at which the three-dimensional axisymmetry breaking of the flow occurs; by three-dimensional numerical simulation, we will study the three-dimensional patterns appearing beyond these thresholds and their further transitions. A finite volume approach based on multigrid SIMPLE scheme is used for the computation of steady states, while an improved fraction-step finite difference method is used for the oscillatory cases. These numerical methods are described in section 3 after the presentation of the mathematical model. The results are then given through the different flow patterns obtained in the different ranges of values of the aspect ratio. The instability mechanisms are then analyzed through mode decomposition techniques and energy transfer analysis. Comparisons with the experimental results[9] are finally given and discussed.

II. MATHEMATICAL MODEL

We consider an incompressible Newtonian fluid confined in a vertical cylindrical cavity of aspect ratio $A = H/R$, where H is the height and R is the radius of the cavity (see Fig. 1). At all the boundaries, no-slip conditions are applied. Following the experimental conditions reported in Ref.[9], the top and bottom of the cylinder are assumed isothermal and held at a low temperature T_c, the central section of the sidewall ($H/2 - R/2 \leq z \leq H/2 + R/2$) is maintained at a high temperature T_h, and the other parts of the sidewall are considered to be adiabatic. All the physical characteristics are taken as constant, except the density which, according to the Boussinesq approximation, is taken as a linear function of temperature in the buoyancy term, $\rho = \rho_0(1 - \beta(T - T_0))$, where β is the thermal expansion coefficient and T_0 the reference temperature ($T_0 = T_c$).

The governing equations for the temperature T, the pressure p and the velocity $\boldsymbol{u}$ are the Navier-Stokes equations coupled with the energy equation. The length, time, velocity and pressure are scaled by R, R^2/α, α/R, $\rho(\alpha/R)^2$, respectively, where α is the thermal diffusivity. Nondimensional temperature is defined by $\theta = (T - T_0)/(T_h - T_c)$. The nondimensional governing equations with Boussinesq approximation in cylindrical coordinates (r, φ, z) can be written as

$$\nabla \cdot \boldsymbol{u} = 0 \tag{1}$$

$$\frac{\partial \boldsymbol{u}}{\partial t} + \boldsymbol{u} \cdot \nabla \boldsymbol{u} = -\nabla p + Pr \nabla^2 \boldsymbol{u} + Pr\, Ra\, \theta\, \widehat{\boldsymbol{z}} \tag{2}$$

$$\frac{\partial \theta}{\partial t} + \boldsymbol{u} \cdot \nabla \theta = \nabla^2 \theta \tag{3}$$

where $Pr = \nu/\alpha$ is the Prandtl number, ν is the kinematic viscosity, $Ra = g\beta(T_h - T_c)R^3/(\alpha\nu)$ is the Rayleigh number, g is the gravity acceleration, and $\widehat{\boldsymbol{z}}$ is the unit vector in the z direction. φ is such that $\varphi = 0$ *deg.* on the positive part of the x-axis and $\varphi = 90$ *deg.* on the positive part of the y-axis. In the axial cross-section views, the x-direction is east (0 *deg.* for φ) and the y-direction is north (90 *deg.* for φ).

The dimensionless boundary conditions can be written as follows:

$$\boldsymbol{u} = 0 \quad \text{on all the boundaries} \tag{4}$$

$$\frac{\partial \theta}{\partial n} = 0 \quad \text{at} \quad r = 1; \quad z < A/2 - 1/2 \quad \text{or} \quad z > A/2 + 1/2 \tag{5}$$

$$\theta = 0 \quad \text{at} \quad z = 0 \quad \text{and} \quad z = A \tag{6}$$

$$\theta = 1 \quad \text{at} \quad r = 1 \quad \text{and} \quad A/2 - 1/2 \leq z \leq A/2 + 1/2 \tag{7}$$

The initial conditions are specified by zero velocity field, and by zero temperature field except on the boundary. In some cases, a random perturbation with small amplitude is used for oscillatory flow calculations. Following the experiment of Ref.[9], the parametric study is performed in the parameter space defined by the Rayleigh number and the aspect ratio.

III. NUMERICAL METHODS

To solve the governing equations, we use two different methods. A finite volume approach based on multigrid SIMPLE scheme is used for the computation of steady states with a quick convergence, while a fraction-step finite difference method with accurate time-stepping is used for the oscillatory cases.

A. Steady state solver

The governing equations are discretized on a structured grid in cylindrical coordinates. The velocity components and the scalar variables (pressure, temperature) are located on the grid in a collocated manner. We use a pressure-based flow solver[12] which is based on the SIMPLE algorithm[13]. Uniform meshes are employed in the azimuthal direction, while a nonuniform grid is used in the radial and axial directions with mesh points concentrated towards the boundaries and the heated region.

In order to overcome the difficulties of a slow convergence, a multigrid acceleration is implemented. The full approximation scheme (FAS) proposed by Brandt[14] and which has been widely used[12], is adopted here. The detailed description of SIMPLE and FAS can be found in Ref.[12].

B. Unsteady time-splitting method

To accurately simulate the unsteady oscillatory convection, a time-splitting finite difference method, also known as fractional-step method[15], is used in cylindrical coordinates[16]. A mixed three-step Runge-Kutta/Crank-Nicholson algorithm is used to solve the equations (1-3). The time discretization for the viscous term is based on a second order Crank-Nicholson scheme, and a third order Runge-Kutta method is used for the advective terms. A central difference method on a staggered grid is used for spatial discretization. The method can then achieve second order in time and space. The advantage of this method is that the treatment of the boundary conditions for the intermediate velocity field is simple, the computer memory used is small and the speed, without iterative solver, is very high.

In natural convection in cylindrical containers, the azimuthal velocities near the axis may be large. Thus, there is a significant stability limit for the selection of the time step Δt. In fact, the azimuthal contribution to the CFL limit is the biggest for oscillatory convection and about 10 times that obtained for the two other directions. So a fully implicit treatment in the azimuthal direction is employed to overcome this difficulty and speed up the calculation.

C. Validation of numerical techniques

Validations through mesh refinement studies have been done for the finite volume SIMPLE method and finite difference method by a steady flow calculation at $A = 4$, $Ra = 700$ and $Pr = 0.021$. The solution corresponds to a steady asymmetric flow. Three mesh levels have been tested on a similar stretched grid which is concentrated near the boundaries and the heated region. The results are given in Table I through the maximum velocities in the azimuthal and vertical directions, the total kinetic energy, and the heat transfer rate at the top plate, namely the Nusselt number (at $r = 0.5$), $\mathrm{Nu} = \frac{1}{2\pi}\int_0^{2\pi}\left(-\frac{\partial \mathrm{T}}{\partial \mathrm{z}}\right)_{\mathrm{z=A}} \mathrm{d}\varphi$, and the average Nusselt number, $\overline{\mathrm{Nu}} = \frac{1}{\pi}\int_0^{2\pi}\int_0^{1}\left(-\frac{\partial \mathrm{T}}{\partial \mathrm{z}}\right)_{\mathrm{z=A}} \mathrm{rdrd}\varphi$. A further validation of the calculation of the heat transfer rate at the top plate is shown in figure 2 through the local Nusselt number which is given as a function of the azimuthal angle φ for $r = 0.75$ (radial position where the local Nusselt number shows the highest values). In any case, between the three mesh levels, the variation of the selected variables is small and the difference is generally under 1%.

D. Mode decomposition

In order to analyse the solutions, it is interesting to decompose them into their main azimuthal Fourier components defined for a variable ϕ as

$$\widehat{\phi}(k, r, z, t) = \frac{1}{N_\varphi} \sum_{j=0}^{N_\varphi - 1} \phi(\varphi, r, z, t)\, e^{-i\, 2\pi\, kj/N_\varphi}. \tag{8}$$

The 0th Fourier mode represents the axisymmetric component of the flow and the other modes are the asymmetric components. The relative intensity of the different modes can also be globally estimated through the flow kinetic energy contained in each azimuthal Fourier mode k:

$$E_{3D}(k, t) = \iint \left|\widehat{\boldsymbol{u}}(k, r, z, t)\right|^2 \, r dr dz \tag{9}$$

where $\widehat{\boldsymbol{u}}(k, r, z, t)$ is the velocity field in the kth Fourier mode.

IV. RESULTS

The flows obtained in vertical cylinders partially heated from the side (fixed length of heated region) correspond for low Rayleigh numbers to axisymmetric toroidal flows near the heated zone. For large A geometry (Fig. 3(c,d)), the convective vortex is confined around this heated zone, and the motions near the top and bottom are very weak. In the upper part, the fluid is heated from below and then unstably stratified, while in the lower part, the fluid is heated from above and then thermally stable. For small A geometry (Fig. 3(a,b)), the fluid motion nearly extends in the whole cylinder, and there is no quiescent thermally unstable region as for larger A.

As has been shown by Rubinov *et al.*[11] the flows which will bifurcate from these toroidal flows will break the axisymmetry property. More precisely, they have shown that, depending on the aspect ratio of the cavity, different perturbation modes (defined by their azimuthal wave number k) are associated with this axisymmetry breaking. For $2 \leq A \leq 2.87$, the critical mode is an oscillatory mode with $k = 2$, for $2.87 \leq A \leq 2.9$ it is an oscillatory mode with $k = 1$, and for $2.9 \leq A \leq 8$ it is a steady mode with $k = 1$. They also indicate that both oscillatory modes at small A correspond to instabilities of hydrodynamic origin whereas the steady mode at larger A corresponds to a Rayleigh-Bénard instability triggered in the upper part of the cylinder where the fluid is unstably stratified.

We present in the following the developed three-dimensional states we have obtained beyond the thresholds by three-dimensional non-linear steady and unsteady calculations for different ranges of the apect ratio A. We first give the spatial patterns obtained, with their temporal properties, then characterized them by energy transfer analysis, and at last present a comparison between the numerical results and the experimental results of Selver *et al.*[9].

A. Patterns developing beyond the axisymmetry breaking

1. Supercritical Hopf bifurcation for $2 \leq A \leq 2.5$

Non-linear time-dependent calculations have been performed for this range of A and oscillatory periodic behaviours have been obtained for Ra above the axisymmetry-breaking threshold. The amplitude of the oscillations for Ra near this critical threshold (denoted as Ra_{cr}) has been checked to be proportional to $(Ra - Ra_{cr})^{1/2}$ indicating a transition to the oscillatory flow through a supercritical Hopf bifurcation. Concerning the period of these oscillatory flows, near the thresholds, they are close to those obtained by stability analysis by Rubinov *et al.*[11]. For example, for the aspect ratio $A = 2$, the threshold given by Rubinov *et al.*[11] is around $Ra_{cr} = 2000$ and the nondimensional oscillation period obtained through the simulations at $Ra = 2100$ is 4.6, a value which is very close to the value 4.53 deduced from their stability analysis. An analysis of the oscillatory flow using Fourier decomposition has also been performed for this case. It shows that the leading non-axisymmetric mode is a $k = 2$ mode, which also corresponds to the critical perturbation mode found by stability analysis by Rubinov *et al.*[11]. In fact, using the kinetic energy E_{3d}, it has been observed that the non-zero even modes have an amplitude decaying exponentially with the order of the mode, whereas the odd modes have zero amplitude.

The flow pattern resulting from the combination of the basic mode $k = 0$ and the main fluctuation $k = 2$ is a kind of two-roll structure with the flow going down near the axis and going up preferentially in two zones oppositely situated along the vertical sidewall (Fig. 4). The oscillatory flow is a travelling wave corresponding to the rotation of the two-roll structure around the cylinder axis. Due to the symmetry properties of the $k = 2$ mode, the fundamental period of the travelling wave corresponds to a π rotation of the flow structure.

2. Multi-state coexistence for $2.7 \leq A \leq 2.9$

A complicated hysteresis (multiplicity of steady and oscillatory states) is observed in the interval $2.7 \leq A \leq 2.9$ by direct numerical simulation. From the linear analysis[11], the transition for these aspect ratios is from the steady axisymmetric flow to an oscillatory flow, but this oscillatory flow is either triggered by the mode $k = 2$ ($2.7 \leq A \leq 2.87$) or by the mode $k = 1$ ($2.87 \leq A \leq 2.9$). For the direct numerical simulation, the final stable oscillatory flow pattern above Ra_{cr} is triggered by a $k = 1$ mode perturbation which is identified by mode decomposition of the solution. Fig. 5 gives the bifurcation diagram near the axisymmetry breaking for the aspect ratio $A = 2.9$. Increasing the Rayleigh number from an axisymmetric state, the flow pattern will be preserved until $Ra_{cr} = 2375$ (given by the stability analysis and indicated by the right dashed-line in Fig. 5) is reached, and then the flow will transit to the oscillatory state with $k = 1$ (O branch in Fig. 5). Now with the decrease of the Rayleigh number, the flow will still be oscillatory down to $Ra = 2050$, and then change to an asymmetric steady branch $A2$. A low frequency branch V is observed in the range $1740 \leq Ra \leq 1860$. Then, as Ra is decreased, there is a jump to the asymmetric steady branch $A1$. The flow patterns of branches $A1$ and $A2$ are similar, and all the flow patterns for the different branches have a strong $k = 1$ component beside the $k = 0$ basic mode. As Ra is further decreased, the flow will transit from the asymmetric steady state $A1$ to the axisymmetric state at $Ra_b = 1310$ (the left dashed-line in Fig. 5). The value Ra_b at which the axisymmetric mode is retrieved when decreasing Ra from supercritical states is given in table II for A between 2.7 and 2.9. From these values, we see that the width of the hysteresis domain is decreased when A is decreased. The existence of such multiple states associated to different solution branches is very similar to what was found in the case of the two dimensional cavity partially heated from the side[10]. This multiplicity was proposed to be the result of the combined mechanisms involved in the present situation: the hydrodynamic instability of the toroidal flow, the Rayleigh-Bénard instability inside the unstably stratified upper part of the cylinder and the flow damping inside the stably stratified lower part.

3. Pitchfork bifurcation for $A \geq 3$

A steady axisymmetry-breaking pitchfork bifurcation has been found by linear stability analysis by Rubinov *et al.*[11] for aspect ratio $A \geq 2.9$, and this bifurcation is associated to a $k = 1$ mode. Three-dimensional numerical simulations have been performed for states slightly above the thresholds for $A \geq 3$. The three-dimensional flow patterns associated to the bifurcated solution and to the main modes obtained by mode decomposition are shown in Figs. 6-9 for $A = 4$ and $A = 8$.

For the larger aspect ratio (case $A = 8$ with $Ra = 400$) shown in Fig. 6, an unicellular flow appears in the upper half of the cylinder, and it interacts with the existing toroidal flow near the heated zone. The orientation of this unicellular flow is arbitrary, but in practice it is given by the perturbations which have triggered the instability. For the calculation presented in Fig. 6, the main flow plane is close to the plane $x = 0$. This main flow plane is a plane of symmetry for the steady flow triggered at the pitchfork bifurcation. This supercritical steady asymmetric flow can be decomposed into the basic axisymmetric flow and the main asymmetric perturbation modes (Fig. 7). The mode with maximum amplitude is a $k = 1$ mode, which is consistent with the linear stability result of Rubinov *et al.*[11]. All the asymmetric modes (Fig. 7) are concentrated in the upper part of the cylinder, where the flow is unstably stratified, similarly to what was found for the perturbation at the threshold by Rubinov *et al.*[11], and indicating a thermal instability. Moreover, the $k = 1$ perturbation component obtained by mode decomposition is very similar to the critical mode given by Rubinov *et al.*[11]. As a result of the perturbations, the isotherms in the upper half become quite strongly distorted (Fig. 6(a)), while those in the lower half are almost undisturbed (the nondimensional temperature difference in the cross-section $z = 0.25H$ is less than 0.001 whereas it is more than 0.02 at $z = 0.9H$).

For the smaller aspect ratio (case $A = 4$ with $Ra = 700$) shown in Fig. 8, the axisymmetric toroidal flow is distorted by the convection roll in the upper half of the cavity in a similar manner as for the larger aspect ratio. But the asymmetric modes components (Fig. 9) extend now into the whole cylinder. The mode with maximum amplitude is still $k = 1$, and this mode is here also very similar to the perturbation pattern given by Rubinov *et al.*[11]. The kinetic energy amplitudes of the asymmetric modes decay exponentially with the order of the modes. Concerning the temperature perturbations connected to the asymmetric mode $k = 1$ (Fig. 9(b)), they present in the upper part a maximum which is two-time larger than that in the lower part. A similar remark can be done for the azimuthal velocity. It seems then that the thermal instability is still dominant in this axisymmetry-breaking transition for $A = 4$.

4. Comparison with the case heated from below for large aspect ratios

As we have seen that the axisymmetry-breaking transition for large aspect ratios seems to be connected to a thermal instability related to the unstably stratified upper part ($z > A/2 + 1/2$), it was worth comparing the thresholds obtained in the cylinder partially heated from the side with the Rayleigh-Bénard thresholds obtained in a cylinder heated from below with a size equal to this upper part (the corresponding aspect ratio is then $A_b = A/2 - 1/2$). First, for the aspect ratios $A_b \geq 1.1$, the critical mode for the Rayleigh-Bénard situation is also the mode $k = 1$[6]. Moreover, the thresholds for the Rayleigh-Bénard situation in a cylinder have been calculated for large variations of the aspect ratio by Charlson and Sani[17] and by Buell and Catton[18]. In both papers, the thresholds for the mode $k = 1$ and large aspect ratios (height over radius) which we are interested in, are given as critical curves from which it is difficult to extract precise data. But in another paper of Buell and Catton[19], numerical data can be found which are given in table III. These data can then be compared with the results of Rubinov *et al.*[11]. For $A_b = 2$ (heated from below), the critical Rayleigh number is $Ra_{cr}(A_b = 2) = 471.25$ which agrees very well with $Ra_{cr}(A = 5) = 473$ (value extracted from Rubinov *et al.*[11]) for the case partially heated from the side. In fact, the Rayleigh-Bénard thresholds seem to be very similar (a little smaller) to those of Rubinov *et al.*[11] for larger aspect ratios ($A \geq 5$), whereas for smaller aspect ratios clear differences appear, the Rayleigh-Bénard thresholds becoming quickly stronger. This is coherent with the fact that for large aspect ratios the upper part is really a quiescent unstably stratified zone as in the Rayleigh-Bénard situation, whereas for smaller aspect ratios the motions generated by the middle zone heating are present in the upper part.

B. Kinetic energy transfer analysis

In order to understand the physical mechanisms responsible for the axisymmetry-breaking transitions for the different aspect ratios, we analyze the kinetic energy transfer around the different bifurcation points. For that we express the bifurcated solution as the sum of a basic state ($\boldsymbol{v}^0$,θ^0) and a perturbation ($\boldsymbol{v}'$,θ'). We then derive the equation expressing the rate of change of the total kinetic energy dK/dt which is given by:

$$\begin{aligned}
\frac{dK}{dt} &= \frac{d}{dt}\int_\Omega \frac{1}{2}\boldsymbol{v}'\boldsymbol{v}'\,d\Omega = -\int_\Omega \boldsymbol{v}'\cdot(\boldsymbol{v}'\cdot\nabla\boldsymbol{v}^0)d\Omega - Pr\int_\Omega (\nabla\times\boldsymbol{v}')^2\,d\Omega + Pr\,Ra\int_\Omega v'_z\,\theta' d\Omega \\
&= -\int_\Omega \left(v'_r v'_r \frac{\partial v^0_r}{\partial r} + v'_r v'_z \frac{\partial v^0_r}{\partial z} + v'_z v'_r \frac{\partial v^0_z}{\partial r} + v'_z v'_z \frac{\partial v^0_z}{\partial z} + \frac{v'_\varphi v'_\varphi v^0_r}{r} \right) d\Omega \\
&\quad - Pr\int_\Omega (\nabla\times\boldsymbol{v}')^2\,d\Omega + Pr\,Ra\int_\Omega v'_z\,\theta' d\Omega \\
&= K_v + K_d + K_b = K_{v1} + K_{v2} + K_{v3} + K_{v4} + K_{v5} + K_d + K_b, \qquad (10)
\end{aligned}$$

In this kinetic energy equation, K_v and K_b represent the perturbation kinetic energy related to the shear of mean flow and to buoyancy forces, respectively, and K_d is the viscous dissipation of the perturbation kinetic energy.

1. Transition to a steady asymmetric state

To analyze the transition from the basic axisymmetric state to a steady asymmetric state, we decompose this steady state beyond the threshold into its basic axisymmetric component ($k = 0$) and the contributions of the other modes, and use these two components as basic state ($\boldsymbol{v}^0$,θ^0) and perturbation ($\boldsymbol{v}'$,θ'), respectively, inside the energy equations. The results of the analysis are given for two cases, one corresponding to a large aspect ratio ($A = 8$) and the other to a smaller aspect ratio ($A = 4$).

For the larger aspect ratio $A = 8$, the axisymmetric flow will transit to a steady asymmetric flow at $Ra_{cr} \approx 380$. The basic axisymmetric flow for this case is similar to the flow presented in Fig. 3(c,d) for $Ra = 300$ and showing the quiescent, unstably stratified upper part. Fig. 10(a) gives the normalized main perturbation kinetic energy contributions as a function of Ra, beyond the threshold. The buoyancy term K_b is the dominant and most destabilizing term as in the case heated from below. The terms connected to shear of the mean flow are really very weak, except K_{v3} (radial gradient of vertical velocity) which contributes up to 10% in the balance, but with a negative sign indicating a stabilizing contribution. All this confirms that the transition is really connected to a thermal instability in this case. The fact that the thresholds are a little above those obtained in the situation heated from below could be connected to the stabilizing term K_{v3}.

For the smaller aspect ratio $A = 4$, the axisymmetric flow will transit to a steady asymmetric flow at $Ra_{cr} \approx 670$. The basic axisymmetric flow for this case is similar to the flow presented in Fig. 3(a,b) for $Ra = 600$ and showing an extension of the convection in the whole cavity. The normalized main perturbation kinetic energy contributions are given as a function of Ra in Fig. 10(b). We see that all terms K_v and K_b are now destabilizing and counter-balance the viscous dissipation term. Among the shear terms, K_{v3} is still the dominant, but now strongly destabilizing. K_{v3} is even stronger than the buoyancy term close to the threshold, but it decreases as Ra is increased, so that K_b becomes quickly the dominant destabilizing term. All this indicates that the transition is still connected to a thermal instability, but that shear effects also have an influence on the development of the instability in this case, particularly close to the thresholds. This can explain why the thresholds become smaller than in the Rayleigh-Bénard situation.

As a conclusion, the dominant mechanism responsible for the axisymmetry breaking to a steady asymmetric state is a thermal instability connected to buoyancy effects in the unstably stratified upper part, but as the aspect ratio is decreased the shear terms play a more and more important role in the development of the instability.

2. Transition to an oscillatory state

In the case of a transition to an oscillatory state, this oscillatory state beyond the threshold is decomposed into its mean value in time and the oscillatory fluctuations which are introduced in the kinetic energy equation (10) as basic state and perturbation, respectively. We analyse the case $A = 2$, which is a typical example for the axisymmetry breaking to oscillatory state, and consider the flow for $Ra = 2100$, a value just above the oscillatory threshold $Ra_{cr} \approx 2000$.

Fig. 11 gives the kinetic energy fluctuation analysis. It is clear from this figure that the production of fluctuating kinetic energy K_v by shear of meanflow is the dominant destabilizing term, much larger than the term of production K_b by buoyancy. This confirms that the transition is connected to a hydrodynamic instability. Among the shear terms, the largest terms K_{v3} and K_{v1}, connected to the radial transport of the radial gradient of the mean velocity, are destabilizing, whereas K_{v2} and K_{v4}, connected to the axial transport of the axial shear, are stabilizing, due to the presence of the end walls.

C. Comparison with experimental results and further transitions

Experimental results on natural convection in a vertical cylinder partially heated from the side have been obtained by Selver *et al.*[9]. They gave the results for different aspect ratios, particularly for $A = 8$ and $A = 4$. For $A = 8$, they mentioned a first steady axisymmetry-breaking transition at $Ra_{cr1}^{exp} \sim 510$ and a further oscillatory transition at $Ra_{cr2}^{exp} \sim 1310$. They also gave the temperature data measured at the cylinder sidewall for $Ra = 1110$ (asymmetric steady state) and for $Ra = 1450$ (oscillatory state). For $A = 4$, they mentioned a direct transition from steady axisymmetric flow to oscillatory asymmetric flow at $Ra_{cr2}^{exp} = 1410$ and gave the oscillatory temperature data obtained for $Ra = 2030$. We present now some comparisons between our numerical simulations and these experimental results.

1. Case $A = 8$

Our direct numerical simulations show a qualitative agreement with the experiment for $A = 8$: our results predict a steady axisymmetry-breaking bifurcation at $Ra_{cr1} = 380$, and a further supercritical Hopf bifurcation at $Ra_{cr2} = 810$. Nevertheless these critical values are clearly below the experimentally observed values. Unsteady time evolutions have also been done for $Ra = 1450$ and $Ra = 1110$, values for which experimental temperature data are given.

For $Ra = 1450$, we obtain an oscillatory state as in the experiment. The period of the oscillatory flow obtained numerically is equal to 2.6 (non-dimensional time, scaled by R^2/α, where $R = 0.955 \times 10^{-2} m$, $\alpha = 1.60 \times 10^{-5} m^2/s$ for gallium at 37°C) corresponding to about 15 seconds. This value is close to the experimental period which is given as 10 seconds[9]. Fig. 12(a) shows the time variations of temperature at eight points on the sidewall ($\varphi = 0, 90, 180, 270\, deg.$, where $\varphi = 0\, deg.$ denotes $x = R, y = 0$, for two heights, $z = 0.875H$ and $z = 0.125H$). As in the experiment, the oscillation amplitudes in the lower part of the cylinder ($z = 0.125H$) are much smaller than those obtained in the upper part ($z = 0.875H$). Temperature data at 90 and 270 *deg.* show the largest oscillation amplitudes, and they are also 180 *deg.* out of phase from each other. But the temperature difference obtained numerically at $z = 0.875H$ (about 0.2 if we compare temperature values at $\varphi = 0$ and 180 *deg.*) is larger than that (about 0.1) obtained in the experiment. Fig. 13 shows the axial velocity of the flow in the cross-section at $z = 0.875H$ for four times during the period. From these plots, we see that, for the upper part of the cylinder, the fluid globally moves up in the left part (around 180 *deg.* angle) and flows down in the right part (around 0 *deg.* angle). This global flow corresponds to the steady convective roll triggered at $Ra_{cr1} = 380$. In the steady regime (from $Ra_{cr1} = 380$ to $Ra_{cr2} = 810$), this one-roll flow contains a reflection symmetry with respect to the plane of main flow (close to the plane $y = 0$ for the case presented in Fig. 13). The contours given in Fig. 13 indicate that this symmetry is no more valid in the oscillatory regime (it has been broken at the Hopf bifurcation point at Ra_{cr2}), but that this symmetry is preserved between states separated by half a period. In fact, the oscillation patterns correspond to a back-and-forth rotation of the convective roll in the upper part of the cylinder, on both sides of the steady main flow plane (standing wave behaviour). The larger temperature oscillation amplitudes observed at 90 and 270 *deg.* angles on the sidewall can be explained by the fact that the rotation of the roll there affects zones with large azimuthal temperature gradients.

For $Ra = 1110$ which is above the numerical threshold $Ra_{cr2} = 810$, we obtain an oscillatory state whereas the experiment gives a steady asymmetric flow. The numerically computed flow pattern is similar to that obtained at $Ra = 1450$ with oscillations still associated with a back-and-forth rotation of the unicellular structure in the upper half of the cylinder. Fig. 12(b) shows that the temperature difference at the cross-section $z = 0.875H$ for $Ra = 1110$ is a little smaller than for $Ra = 1450$ because of the smaller Rayleigh number involving a temperature field less distorted by the mean flow. The temperature oscillations have quite the same amplitudes, but the oscillation period is larger, about 3.6 corresponding to 21 seconds. The differences between the simulation and the experiment are mainly due to the lower thresholds found in the numerical simulation.

2. Case $A = 4$

For $A = 4$, the experimental results differ from the numerical results, as they give a direct transition from the axisymmetric flow to an oscillatory flow at $Ra_{cr2}^{exp} = 1410$ whereas the numerical results give a first pitchfork bifurcation from the axisymmetric flow to a steady asymmetric unicellular flow at $Ra_{cr1} = 670$, and then a transition to oscillatory flow near $Ra_{cr2} = 1630$. Because of the competition between the inertia and buoyancy forces in this case, the flow transition is more complex. Above $Ra_{cr2} = 1630$, a very low frequency oscillation first appears. But beyond $Ra = 1830$, the situation becomes very similar to the back-and-forth rotation found in the numerical result for $A = 8$, which is different from the experimental result showing that the oscillation pattern is a travelling wave with a rotating flow pattern around the cylinder axis. For comparison, we have done a simulation for $Ra = 2000$, a value close to $Ra = 2030$ for which experimental temperature data are given.

Fig. 14 shows the time variations of temperature at eight points on the sidewall at two heights ($z = 0.75H$ and $z = 0.25H$). The temperature difference in given cross-sections is here also smaller in the lower part of the cylinder ($z = 0.25H$) than in the upper part ($z = 0.75H$), but the oscillation amplitudes, although smaller in the lower part, do not differ so much. In fact, for a given cross-section, the oscillation amplitudes are found much smaller than the temperature difference (for example 0.008 compared to 0.45 for the cross-section at $z = 0.75H$), indicating small flow oscillations compared to the mean flow intensity. The main period of the oscillatory flow obtained numerically is equal to 1.4 (see Fig. 14) corresponding to about 8 seconds, a value close to the experimental period which is given as 10 seconds. Note that the oscillation period at $\varphi = 0$ and 180 *deg.* is one half of that at $\varphi = 90$ and 270 *deg.* because of the symmetric oscillation on both sides of the plane $y = 0$ (this was also valid for the oscillations obtained for $A = 8$). The axial velocity contours given in Fig. 15 confirm that the flow oscillations in this case are weak and do not much affect the mean flow pattern. For this case $A = 4$, there is no agreement on the way to transit to oscillations between experiments and simulations. In fact, what has been found experimentally for $A = 4$, i. e., a direct transition to oscillatory flow and a travelling wave behaviour with a rotating flow pattern, is in better agreement with what has been found numerically for $A = 2$ (see section 4.1.1).

3. Discussion

The comparisons between experimental and numerical results have shown some disagreements. Different reasons can be found to explain these disagreements.

A potential reason for the discrepancy between simulations and experiments could be the variation of the Prantdl number induced in the gallium by the temperature differences[20,21], variation which is not taken into account in the simulations. But, from Rubinov *et al.*[11] it can be stated that this variation has no consequence, as they have shown that the thresholds do not change much when Pr is varied around 0.021. In fact changes have only been found for smaller Pr, with a clear increase of the threshold and even a change of the critical mode below $Pr = 0.002$.

The disagreements could also be related to differences in the thermal boundary conditions[9], as the boundary conditions for the simulations are strict conditions (boundaries either perfectly insulating, or with an imposed temperature) which are difficult to impose exactly in the experiment. To test the influence of these boundary conditions, some calculations have been done in slightly different conditions (hot zone at mid-height with a slight linear variation of the temperature along z, cylinder slightly inclined). These test calculations have given very similar steady flows. Nevertheless, as convective problems are very sensitive to the thermal conditions, we cannot get rid of the influence of thermal conditions in this problem.

In fact, as already proposed by Rubinov *et al.*[11], the differences betwen the experimental and numerical results can be viewed as a shift in A between these results. The imperfections in the experiment (compared to the numerical model) seem to have shifted the experimental results to smaller effective aspect ratios. This could be the case if the effective heated zone was larger than that where the ring heater is applied in the experiment. This shift in A could explain why in the experiment for $A = 4$ there is a direct transition to oscillatory flow and a travelling wave behaviour with a rotating flow pattern, a result found numerically for A between 2 and 2.5. This would also lead us to compare the experimental results for $A = 8$ to the numerical results obtained at smaller A, which gives a better agreement between the values of the thresholds.

V. CONCLUSION

Three-dimensional steady and oscillatory flows have been simulated in a vertical cylinder partially heated from the side. The vertical wall is heated at the mid-height and is insulated above and below the middle zone, while both ends of the cylinder are cooled. The cylinder aspect ratio A ranges from 2 to 8, whereas a fixed Prandtl number, $Pr = 0.021$, is considered.

The basic steady flow that develops in such situation is a toroidal pattern. As shown by Rubinov *et al.*[11] by stability analysis, the first transition breaks the axisymmetry. For $2 \leq A \leq 2.87$, the critical mode is an oscillatory mode with $k = 2$, for $2.87 \leq A \leq 2.9$ it is an oscillatory mode with $k = 1$, and for $2.9 \leq A \leq 8$ it is a steady mode with $k = 1$.

The spatial pattern and temporal properties of the developed three-dimensional states beyond these thresholds have been studied by non-linear steady and unsteady calculations, and the instability mechanisms have been studied by mode decomposition techniques and energy transfer analyses. These results confirm that a hydrodynamic instability is responsible for the onset of oscillations at small A, while the Rayleigh-Bénard mechanism is involved in the transition to a steady asymmetric state at large A in connection with the thermally unstable stratification in the upper half of the cylinder. For small aspect ratio, such as $2 \leq A \leq 2.5$, the onset of oscillations is associated with a supercritical Hopf bifurcation, and the leading non-axisymmetric mode in the resulting flow pattern is $k = 2$, in agreement to what is given at the critical threshold by the stability analysis. The oscillation pattern is a travelling wave corresponding to the rotation of the two roll structure (combination of the axisymmetric basic flow and the $k = 2$ perturbation) around the cylinder axis. A complicated hysteresis phenomenon due to the multiplicity of steady and oscillatory states is then found in the narrow aspect ratio interval $2.7 \leq A \leq 2.9$. For larger aspect ratios $3 \leq A \leq 8$, an unicellular steady flow appears in the upper half of the cylinder beyond the pitchfork bifurcation, which interacts with the existing toroidal flow near the heated zone. This last transition is connected to the Rayleigh-Bénard instability and then, to buoyancy phenomena. For long enough aspect ratios ($A \geq 4.5$), the thresholds even show a good agreement with those calculated for a vertical cylinder heated from below with a height equal to the height of the unstably stratified upper part, whereas for smaller aspect ratios the shear phenomena also have an influence on the thresholds.

Comparisons with the experiments of Selver et al.[9] at the aspect ratios $A = 4$ and $A = 8$ are then considered, which leads to further calculations for these aspect ratios, beyond the pitchfork bifurcation and until the oscillatory transition. A qualitative agreement is obtained at $A = 8$, namely a first pitchfork bifurcation breaking the axisymmetry and leading to a steady unicellular flow, and then a transition to an oscillatory flow characterized by a back-and-forth rotation of the unicellular flow around the cylinder axis. Nevertheless, the value of the thresholds measured experimentally are smaller than those obtained in the numerical calculations. For $A = 4$, there is no agreement between the experiment and the calculations. Calculations predict a transition similar to what has been shown for $A = 8$, whereas the experiment shows a direct transition from steady axisymmetric to oscillatory flows, with the triggering of a rotating pattern. Nevertheless, this experimentally observed transition is similar to what has been found numerically for A between 2 and 2.5. The disagreements observed between experiments and calculations have then been discussed. The best explanation would be a kind of shift in A between these results, the experimental results fitting in a better way the numerical results obtained for smaller aspect ratios.

REFERENCES

[1] G. Müller and A. Ostrogorsky. Convection in melt growth. In D. T. J. Hurle, editor, *Handbook of Crystal Growth*, volume 2, pages 711–781. North-Holland, Amsterdam, 1994.

[2] J. P. Garandet and T. Alboussière. Bridgman growth: modeling and experiments. *Progr. Cryst. Growth and Characterization of Materials*, 38:73, 1999.

[3] G. Müller, G. Neumann, and W. Weber. Natural convection in vertical Bridgman configurations. *J. Crystal Growth*, 70:78–93, 1984.

[4] G. Neumann. Three-dimensional numerical simulation of buoyancy-driven convection in vertical cylinders heated from below. *J. Fluid Mech.*, 214:559–578, 1990.

[5] M. Wanschura, H. C. Kuhlmann, and H. J. Rath. Three-dimensional instability of axisymmetric buoyant convection in cylinders heated from below. *J. Fluid Mech.*, 326:399–415, 1996.

[6] R. Touihri, H. Ben Hadid, and D. Henry. On the onset of convective instabilities in cylindrical cavities heated from below. I. Pure thermal case. *Phys. Fluids*, 11:2078–2088, 1999.

[7] J. Baumgartl, W. Budweiser, G. Müller, and G. Neumann. Studies of buoyancy-driven convection in a vertical cylinder with parabolic temperature profile. *J. Crystal Growth*, 97:9–17, 1989.

[8] A. Yu. Gelfgat, P. Z. Bar-Yoseph, and A. Solan. Axisymmetry breaking instabilities of natural convection in a vertical bridgman growth configuration. *J. Crystal Growth*, 220:316–325, 2000.

[9] R. Selver, Y. Kamotani, and S. Ostrach. Natural convection of a liquid metal in vertical circular cylinders heated locally from the side. *J. Heat Transfer*, 120:108–114, 1998.

[10] V. Erenburg, A. Yu. Gelfgat, E. Kit, P. Z. Bar-Yoseph, and A. Solan. Multiple states, stability and bifurcations of natural convection in a rectangular cavity with partially

heated vertical walls. *J. Fluid Mech.*, 492:63–89, 2003.

[11] A. Rubinov, V. Erenburg, A. Yu. Gelfgat, E. Kit, P. Z. Bar-Yoseph, and A. Solan. Three-dimensional instabilities of natural convection flow in a vertical cylinder with partially heated sidewall. *ASME J. Heat Transfer*, 126:586–599, 2004.

[12] J. H. Ferziger and M. Peric, editors. *Computational Methods for Fluid Dynamics.* Springer-Verlag, Berlin, 1996.

[13] S. V. Patankar, editor. *Numerical Heat Transfer and Fluid Flow.* Hemisphere, Washington, DC, 1980.

[14] A. Brandt. Multilevel adaptative computations in fluid dynamics. *AIAA Paper*, 79:1455, 1979.

[15] J. Kim and P. Moin. Application of a fractional-step method to incompressible Navier-Stokes equations. *J. Comput. Phys.*, 59:308–323, 1985.

[16] R. Verzicco and P. Orlandi. A finite-difference scheme for the three-dimensional incompressible flows in cylindrical coordinates. *J. Comput. Phys.*, 123:402–414, 1996.

[17] G.S. Charlson and R.L. Sani. On thermoconvective instability in a bounded cylindrical fluid layer. *Int. J. Heat Mass Tranfer*, 14:2157, 1971.

[18] J.C. Buell and I. Catton. The effect of wall conduction on the stability of a fluid in a right circular cylinder heated from below. *ASME J. Heat Transfer*, 105:255, 1983.

[19] J.C. Buell and I. Catton. Effect of rotation on the stability of a bounded cylindrical layer of fluid heated from below. *Phys. Fluids*, 26:892, 1983.

[20] B. Hof, A. Juel, L. Zhao, D. Henry, H. BenHadid, and T. Mullin. On the onset of oscillatory convection in molten gallium. *J. Fluid Mech.*, 515:391–413, 2004.

[21] A. Yu. Gelfgat, P. Z. Bar-Yoseph, and A. L. Yarin. Stability of multiple steady states of convection in laterally heated cavities. *J. Fluid Mech.*, 388:315–334, 1999.

Method	Mesh($N_r \times N_\varphi \times N_z$)	$\lvert V_\varphi \rvert_{max}$	$\lvert V_z \rvert_{max}$	E_k	$\overline{Nu}$	$Nu(r = 0.5)$
FVM	$32 \times 32 \times 128$	0.44730	1.51245	1.13360	0.56295	0.56235
FVM	$48 \times 48 \times 192$	0.45256	1.51212	1.13577	0.56394	0.56339
FVM	$64 \times 64 \times 256$	0.45388	1.51184	1.13660	0.56442	0.56388
FDM	$32 \times 32 \times 128$	0.46885	1.50950	1.16186	0.56318	0.56281
FDM	$48 \times 48 \times 192$	0.46326	1.51039	1.15090	0.56405	0.56361
FDM	$64 \times 64 \times 256$	0.46069	1.51089	1.14625	0.56448	0.56401

TABLE I. Mesh refinement tests of numerical accuracy for the steady flow at $Ra = 700$, $Pr = 0.021$ ($A = 4$).

A	Ra_b
2.7	1660
2.8	1480
2.9	1310

TABLE II. Values of the Rayleigh number Ra_b at which the axisymmetric mode is retrieved when decreasing Ra from oscillatory states for A between 2.7 and 2.9.

A_b	(Corresponding A)	Ra_{cr}
1.429	(3.857)	908.95
2	(5)	471.25
2.857	(6.714)	361.01
4	(9)	371.875

TABLE III. Critical thresholds corresponding to $k = 1$ mode for the Rayleigh-Bénard situation in a cylinder and for different aspect ratios (from Buell and Catton[19]).

Figures caption

Figure 1: Geometry of the problem.

Figure 2: Local Nusselt number at the top plate as a function of the azimuthal angle φ (in radians) for $r = 0.75$ ($Ra = 700$, $Pr = 0.021$, $A = 4$): test calculations for different meshes and methods.

Figure 3: Streamlines (a) and isotherms (b) for the axisymmetric flow at $Ra = 600$ for $A = 4$ ($Ra_{cr} = 670$); streamlines (c) and isotherms (d) for the axisymmetric flow at $Ra = 300$ for $A = 8$ ($Ra_{cr} = 380$).

Figure 4: Axial velocity in the cross section $z = 0.875H$ at four times during the period to show the travelling wave oscillatory state obtained for $A = 2$, $Pr = 0.021$ and $Ra = 2100$ (dashed lines correspond to negative values).

Figure 5: Multiplicity of steady and oscillatory states near the axisymmetry-breaking transition for $A = 2.9$: (A1) and (A2) represent steady asymmetric states, (V) is an oscillatory state with low frequency, and (O) is the oscillatory branch emerging at the axisymmetry-breaking threshold.

Figure 6: Flow patterns of the steady asymmetric solution at $A = 8$ and $Ra = 400$: (a) isotherms in four different axial cross-sections, (b) velocity field in the meridian planes ($x = 0$ and $y = 0$).

Figure 7: Mode decomposition of the three-dimensional steady asymmetric flow at $A = 8$, $Ra = 400$ ($Ra_{cr} = 380$): (a-d) are the four leading modes $k = 0, 1, 2, 3$ of the temperature, (e) is the leading mode $k = 1$ of the azimuthal velocity.

Figure 8: Flow patterns of the steady asymmetric solution at $A = 4$ and $Ra = 700$: (a) isotherms in four different axial cross-sections, (b) velocity field in the meridian planes ($x = 0$ and $y = 0$).

Figure 9: Mode decomposition of the three-dimensional steady asymmetric flow at $A = 4$, $Ra = 700$ ($Ra_{cr} = 670$): (a-d) are the four leading modes $k = 0, 1, 2, 3$ of the temperature, (e) is the leading mode $k = 1$ of the azimuthal velocity.

Figure 10: Main fluctuating kinetic energy contributions normalized by K_d for $Pr = 0.021$. (a) $A = 8$, (b) $A = 4$.

Figure 11: Kinetic energy fluctuations analysis for $A = 2$, $Ra = 2100$, $Pr = 0.021$.

Figure 12: Temperature oscillations at eight different locations on the side wall (four azimuthal positions, two heights) for $A = 8$, $Pr = 0.021$ and two values of Ra ($\varphi = 0\, deg.$ denotes the position $x = R$ and $y = 0$). (a) $Ra = 1450$, (b) $Ra = 1110$.

Figure 13: Axial velocity in the cross section $z = 0.875H$ at four times during the period to show the standing wave oscillatory state obtained for $A = 8$, $Pr = 0.021$ and $Ra = 1450$ (dashed lines correspond to negative values).

Figure 14: Temperature oscillations at eight different locations on the side wall (four azimuthal positions, two heights) for $A = 4$, $Pr = 0.021$ and $Ra = 2000$ ($\varphi = 0\, deg.$ denotes the position $x = R$ and $y = 0$). (a) $z = 0.75H$, (b) $z = 0.25H$.

Figure 15: Axial velocity in the cross section $z = 0.875H$ at four times during the period to show the standing wave oscillatory state obtained for $A = 4$, $Pr = 0.021$ and $Ra = 2000$ (dashed lines correspond to negative values).

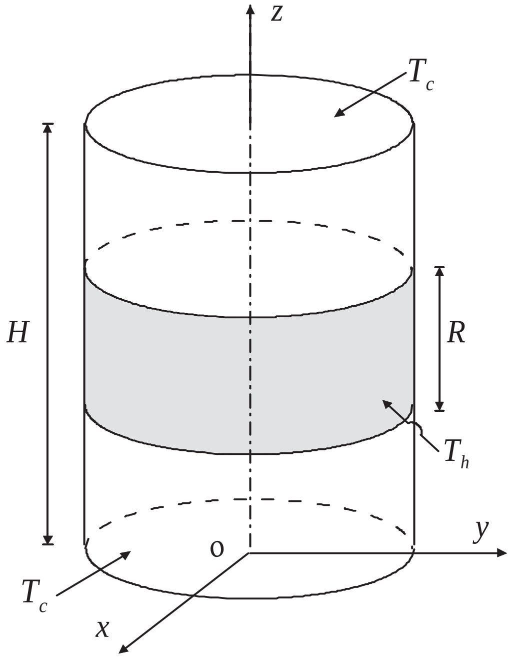

FIG. 1. Geometry of the problem.

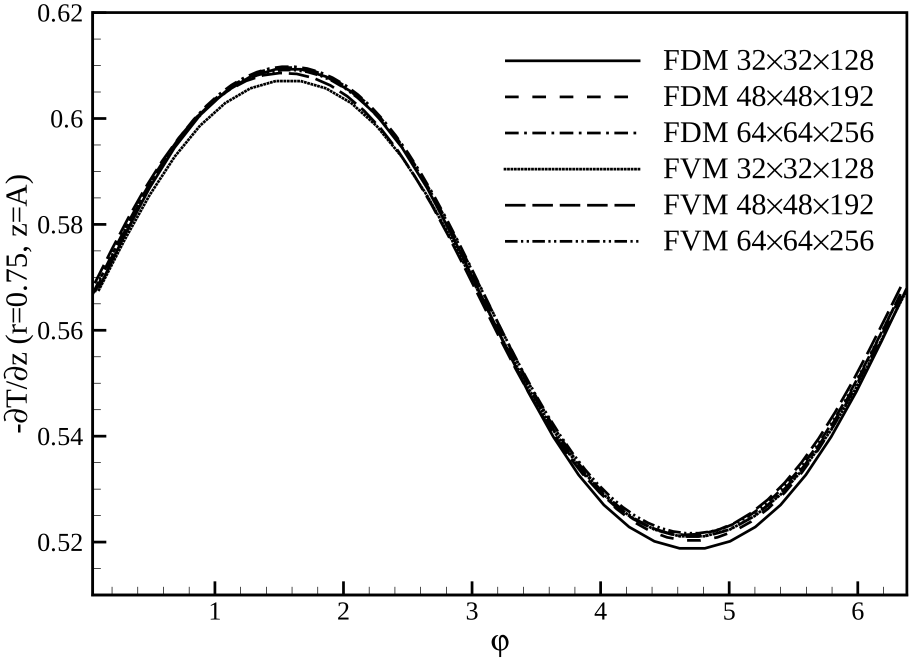

FIG. 2. Local Nusselt number at the top plate as a function of the azimuthal angle φ (in radians) for $r = 0.75$ ($Ra = 700$, $Pr = 0.021$, $A = 4$): test calculations for different meshes and methods.

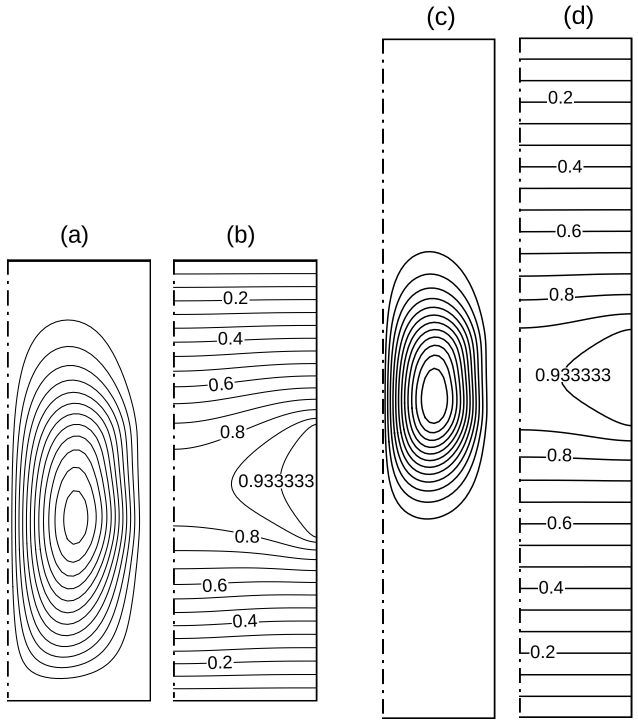

FIG. 3. Streamlines (a) and isotherms (b) for the axisymmetric flow at $Ra = 600$ for $A = 4$ ($Ra_{cr} = 670$); streamlines (c) and isotherms (d) for the axisymmetric flow at $Ra = 300$ for $A = 8$ ($Ra_{cr} = 380$).

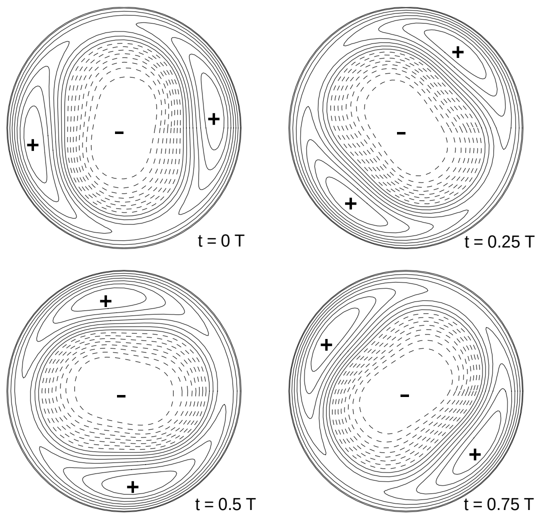

FIG. 4. Axial velocity in the cross section $z = 0.875H$ at four times during the period to show the travelling wave oscillatory state obtained for $A = 2$, $Pr = 0.021$ and $Ra = 2100$ (dashed lines correspond to negative values).

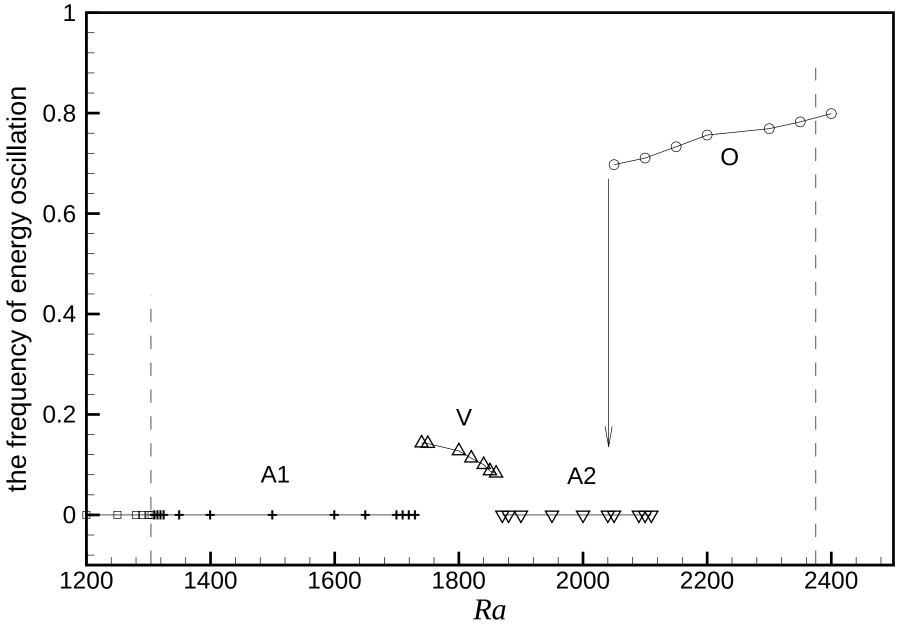

FIG. 5. Multiplicity of steady and oscillatory states near the axisymmetry-breaking transition for $A = 2.9$: (A1) and (A2) represent steady asymmetric states, (V) is an oscillatory state with low frequency, and (O) is the oscillatory branch emerging at the axisymmetry-breaking threshold.

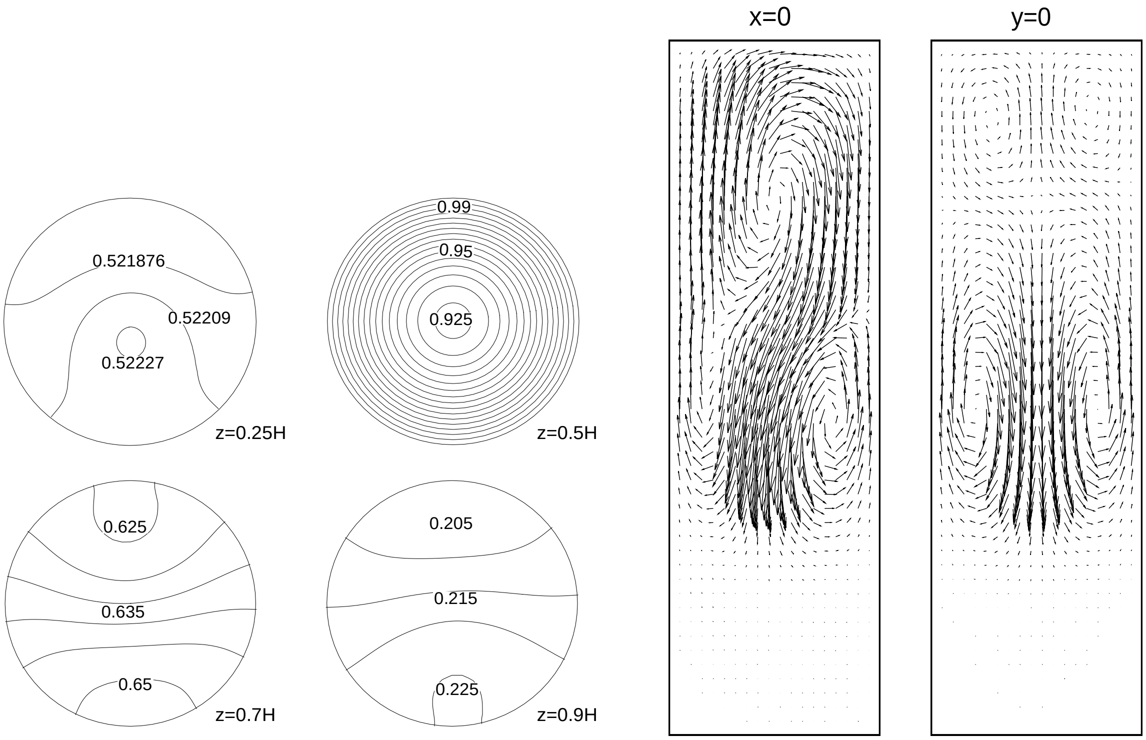

(a) (b)

FIG. 6. Flow patterns of the steady asymmetric solution at $A = 8$ and $Ra = 400$: (a) isotherms in four different axial cross-sections, (b) velocity field in the meridian planes ($x = 0$ and $y = 0$).

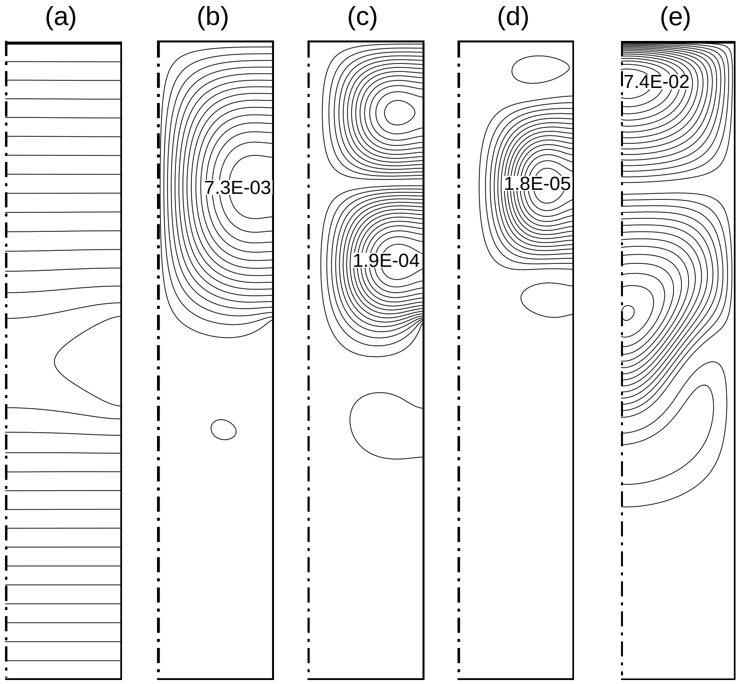

FIG. 7. Mode decomposition of the three-dimensional steady asymmetric flow at $A = 8$, $Ra = 400$ ($Ra_{cr} = 380$): (a-d) are the four leading modes $k = 0, 1, 2, 3$ of the temperature, (e) is the leading mode $k = 1$ of the azimuthal velocity.

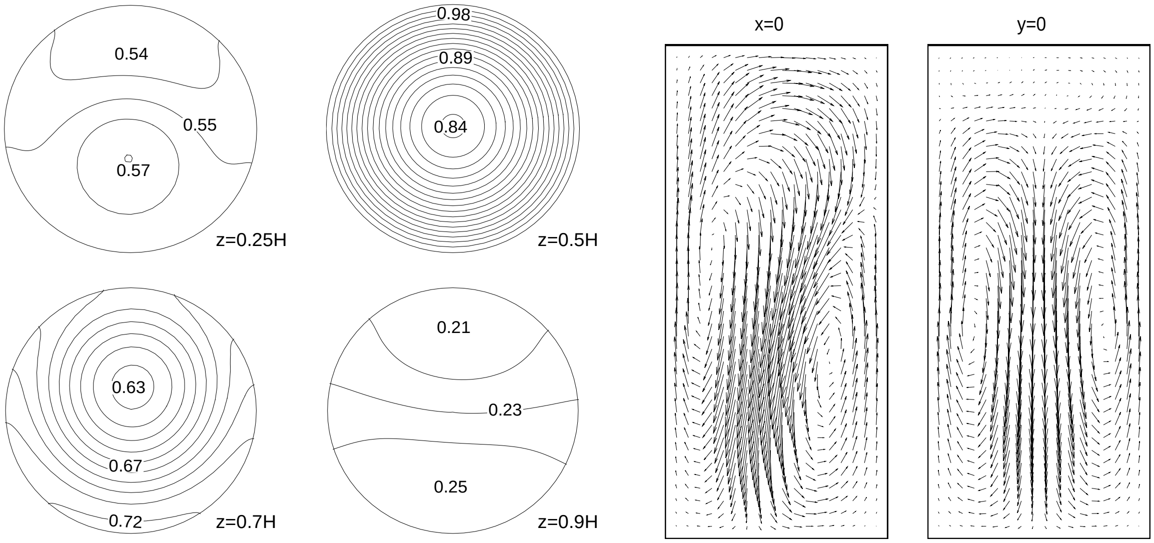

(a) (b)

FIG. 8. Flow patterns of the steady asymmetric solution at $A = 4$ and $Ra = 700$: (a) isotherms in four different axial cross-sections, (b) velocity field in the meridian planes ($x = 0$ and $y = 0$).

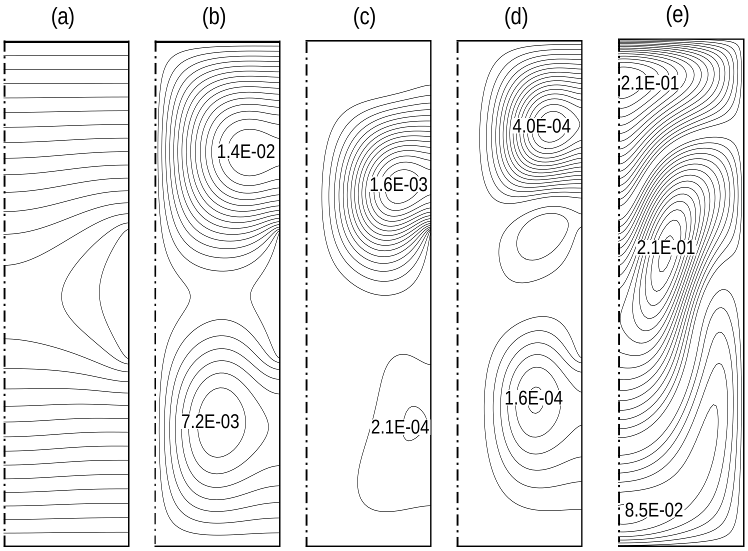

FIG. 9. Mode decomposition of the three-dimensional steady asymmetric flow at $A = 4$, $Ra = 700$ ($Ra_{cr} = 670$): (a-d) are the four leading modes $k = 0, 1, 2, 3$ of the temperature, (e) is the leading mode $k = 1$ of the azimuthal velocity.

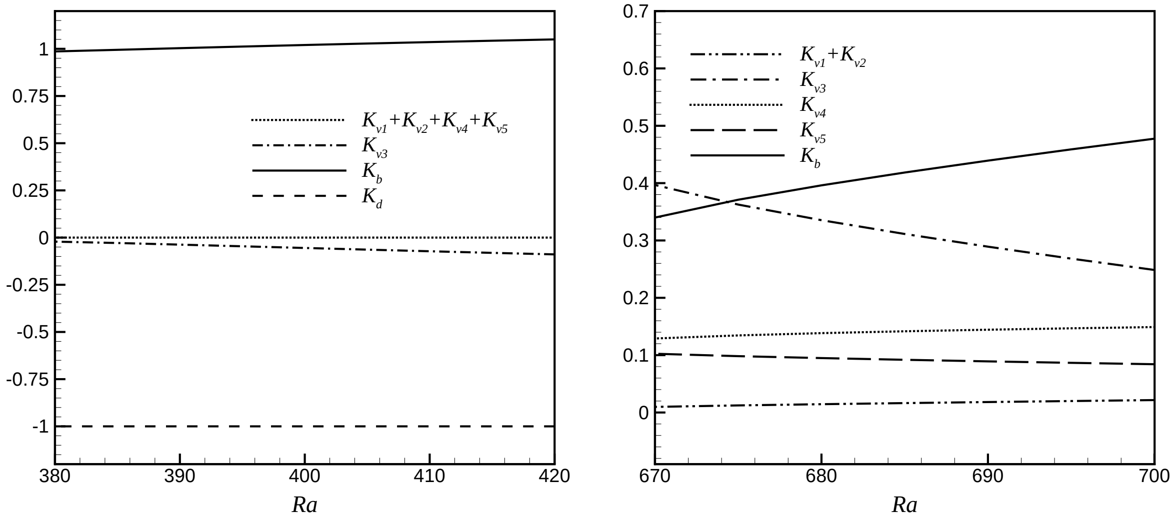

(a) $A = 8$

(b) $A = 4$

FIG. 10. Main fluctuating kinetic energy contributions normalized by K_d for $Pr = 0.021$.

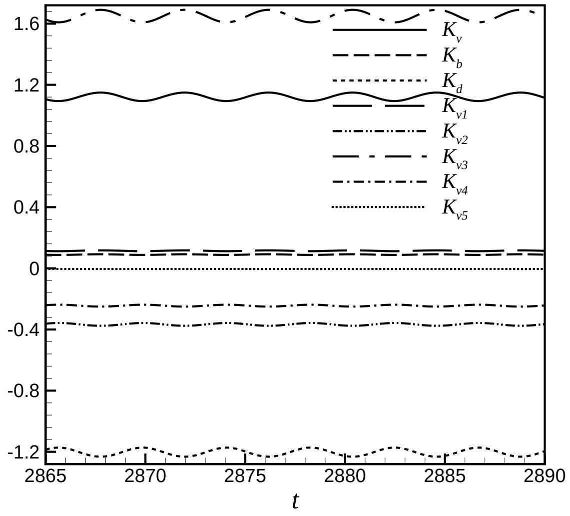

FIG. 11. Kinetic energy fluctuations analysis for $A = 2$, $Ra = 2100$, $Pr = 0.021$.

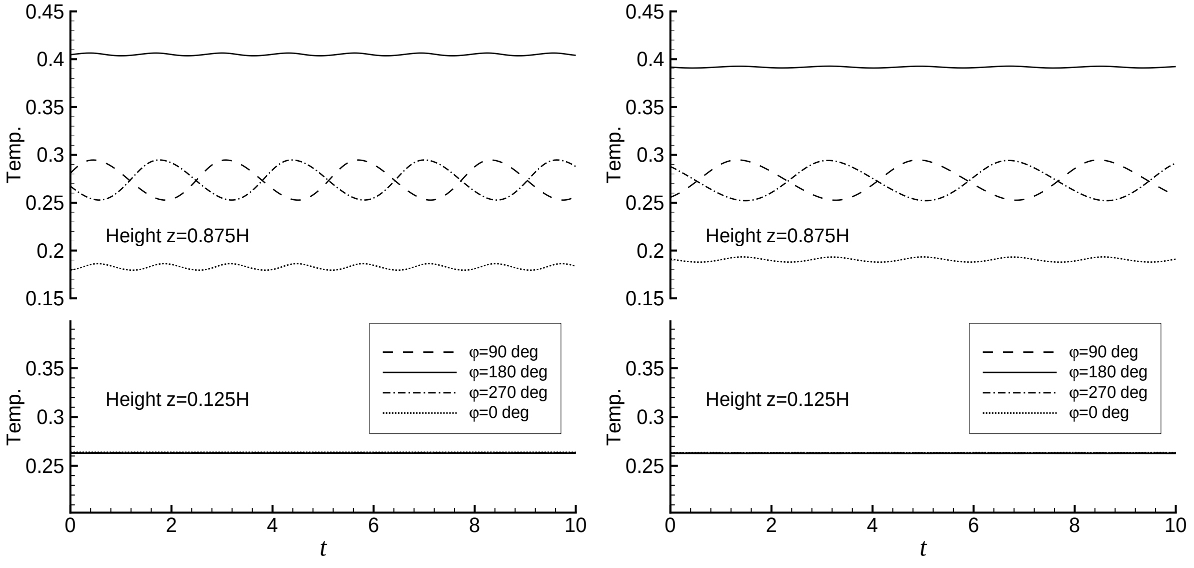

(a) $Ra = 1450$ (b) $Ra = 1110$

FIG. 12. Temperature oscillations at eight different locations on the side wall (four azimuthal positions, two heights) for $A = 8$, $Pr = 0.021$ and two values of Ra ($\varphi = 0\,deg.$ denotes the position $x = R$ and $y = 0$).

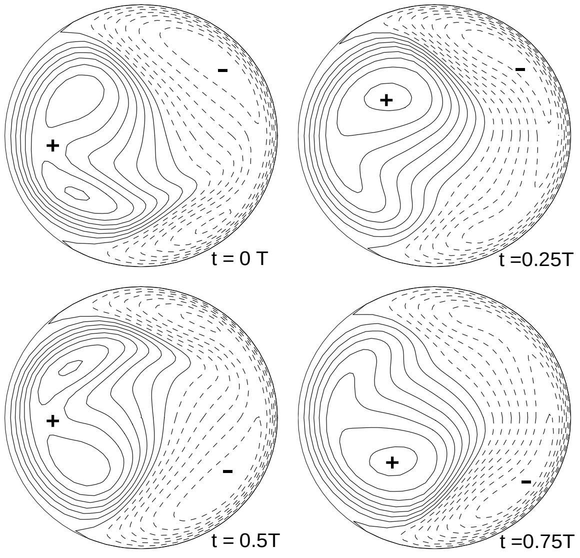

FIG. 13. Axial velocity in the cross section $z = 0.875H$ at four times during the period to show the standing wave oscillatory state obtained for $A = 8$, $Pr = 0.021$ and $Ra = 1450$ (dashed lines correspond to negative values).

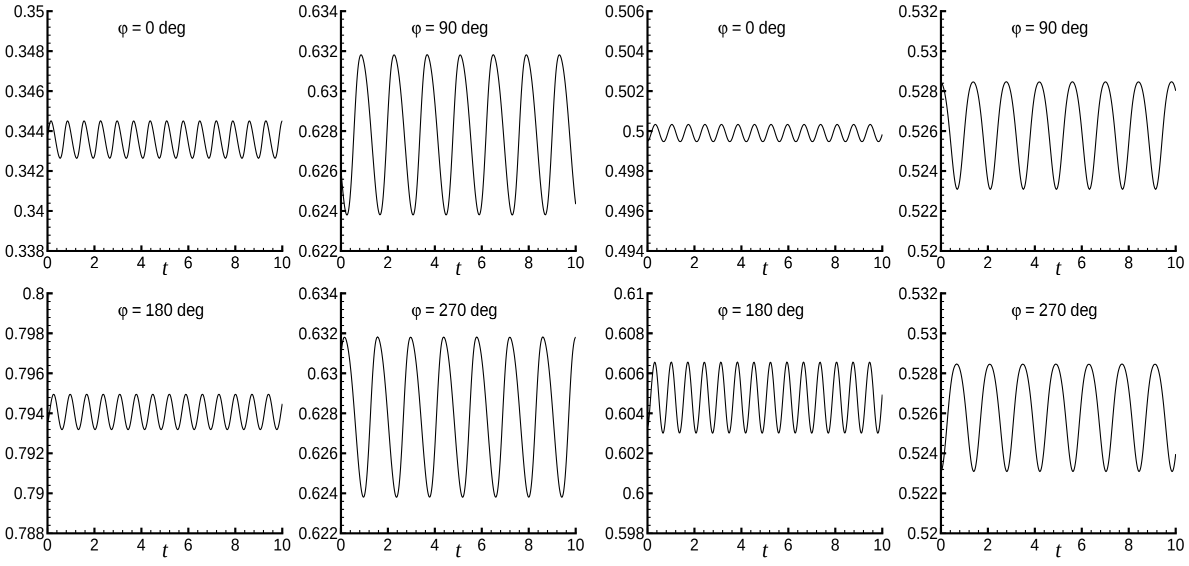

(a) $z = 0.75H$ (b) $z = 0.25H$

FIG. 14. Temperature oscillations at eight different locations on the side wall (four azimuthal positions, two heights) for $A = 4$, $Pr = 0.021$ and $Ra = 2000$ ($\varphi = 0\,deg.$ denotes the position $x = R$ and $y = 0$).

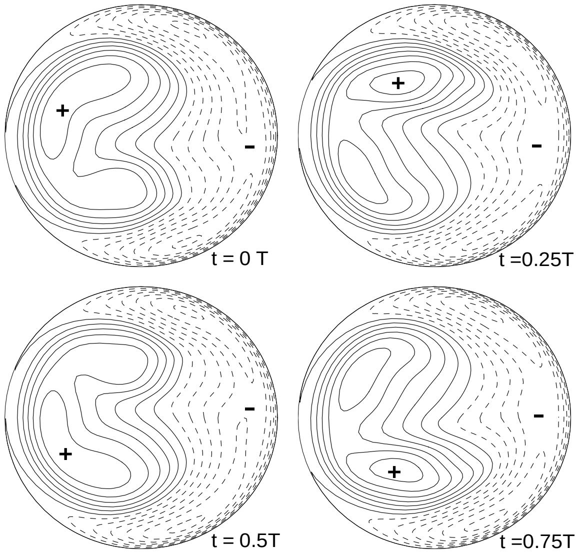

FIG. 15. Axial velocity in the cross section $z = 0.875H$ at four times during the period to show the standing wave oscillatory state obtained for $A = 4$, $Pr = 0.021$ and $Ra = 2000$ (dashed lines correspond to negative values).